Nano Research

Open Access

Research Article

Natural polyphenol modified ZIF boosted the efficiency of berberine for diabetic kidney disease therapy

Hengjie Zhang[1,2,§], Yutong Zou[1,§], Mengxin Wang[2], Ming Gong[2], Haiyan Wang[1], Qing Yang[1], Xingyuan Li[1], Xiaoting Chen[3], Xiting Zou[4], Yiwen Li[2], Zhipeng Gu[2] ✉, and Fang Liu[1] ✉

[1] *Department of Nephrology, West China Hospital of Sichuan University, Chengdu 610041, China*
[2] *College of Polymer Science and Engineering, State Key Laboratory of Advanced Polymer Materials, Sichuan University, Chengdu 610065, China*
[3] *Animal Experimental Center, West China Hospital, Sichuan University, Chengdu 610041, China*
[4] *Hospital of Chengdu Office of People's Government of Tibetan Autonomous Region, Chengdu 610041, China*
§ *Hengjie Zhang and Yutong Zou contributed equally to this work.*

Cite this article: *Nano Research*, **2026**, *19*, 94908761. https://doi.org/10.26599/NR.2026.94908761

ABSTRACT: Diabetic kidney disease (DKD) represents a major diabetes-related complication and is among the most important causes of end-stage renal disease (ESRD). Current therapies mainly focus on glycemic control but seldom reverse established renal injury. Berberine (BBR) shows promise for DKD through glucose-lowering, anti-inflammatory, and antioxidant effects, yet its translation is limited by poor bioavailability and rapid metabolism. Here, we developed ZIF-BBR-BPNs, a nanoparticle system that encapsulates BBR in a zeolitic imidazolate framework (ZIF) core and applies an epigallocatechin gallate (EGCG) coating to improve stability, systemic exposure, and renal enrichment. *In vitro*, ZIF-BBR-BPNs decreased oxidative stress, inflammatory activation, and apoptosis, helping maintain glomerular endothelial cell integrity and function. *In vivo*, the formulation reduced albuminuria and improved renal inflammation, fibrosis, and glomerular damage, with stronger effects than free BBR or metformin. Notably, the formulation increased systemic exposure and enabled passive renal accumulation, supporting sustained therapeutic activity at injury sites. Overall, this multi-target strategy against metabolic stress, oxidative injury, inflammation, and fibrosis enhances BBR efficacy and supports ZIF-BBR-BPNs as a promising candidate for DKD therapy.

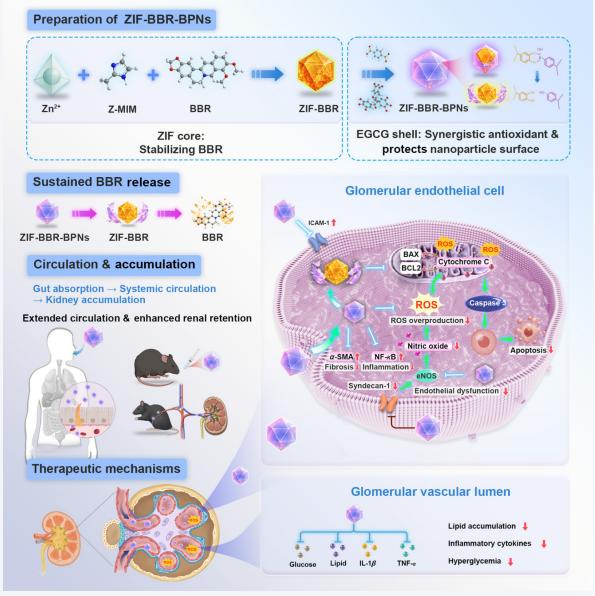

KEYWORDS: natural polyphenol, diabetic kidney disease, berberine, synergistic therapy

1 Introduction

Diabetic kidney disease (DKD) develops in the setting of persistent hyperglycemia and manifests as a gradual decline in renal structure and function [1, 2]. It accounts for a substantial proportion of end-stage renal disease (ESRD) cases worldwide [3]. Current clinical management strategies primarily emphasize stringent glycemic control to mitigate the direct cytotoxic effects of hyperglycemia on renal cells and to slow the progression of renal fibrosis [4, 5]. Although glucose-lowering agents effectively reduce blood glucose levels and may delay early functional decline, they generally exert limited effects on preventing or reversing progressive damage to renal microarchitecture, particularly in the presence of established glomerulosclerosis and tubulointerstitial fibrosis [6, 7]. Although metformin remains a standard first-line antidiabetic drug, evidence for a kidney-reparative effect in established DKD is limited, and it has not been demonstrated to reverse structural injury or recover

Received: March 8, 2026; **Revised:** April 15, 2026
Accepted: April 20, 2026

✉Address correspondence to Zhipeng Gu, guzhipeng2019@scu.edu.cn; Fang Liu, liufangfh@163.com

renal function independent of glycemic control [8, 9]. DKD progression reflects multiple pathogenic inputs beyond hyperglycemia, including dyslipidemia, persistent inflammation, oxidative injury, and disordered renal metabolism [10, 11]. Accordingly, there is growing interest in therapeutic strategies that extend beyond glucose control alone and instead integrate glycemic regulation with lipid modulation and direct renoprotective effects [12]. Pharmacological interventions capable of simultaneously improving metabolic homeostasis and attenuating renal injury may therefore offer a more effective and holistic approach to delaying DKD progression and preserving kidney function [13, 14].

Berberine (BBR) is a natural isoquinoline alkaloid that has attracted attention as a candidate intervention for DKD because of its metabolic benefits and potential renal protection [15, 16]. In addition to its glucose-lowering activity, BBR shows anti-inflammatory and antioxidant actions and has also been reported to exert antitumor effects, mechanisms closely linked to DKD development and progression [17, 18]. Accumulating preclinical evidence indicates that BBR can effectively mitigate DKD progression by improving renal function, suppressing inflammatory responses, and attenuating extracellular matrix accumulation and renal fibrosis [19, 20]. In db/db mouse models, BBR treatment not only improved systemic metabolic profiles but also markedly reduced renal lipid accumulation, highlighting its ability to modulate dysregulated lipid metabolism and protect renal structure and function in DKD [21]. Consistently, a recent meta-analysis confirmed that BBR significantly ameliorates renal function, reduces proteinuria, and suppresses renal fibrosis across multiple animal models of DKD, underscoring its robust renoprotective effects despite current limitations in clinical translation [22–24]. In addition, emerging studies suggest that BBR confers renal benefits through modulation of gut microbiota composition and reduction of uremic toxin production in chronic kidney disease, further supporting its pleiotropic mechanisms of action in renal protection [25, 26]. Despite these promising therapeutic effects, the clinical application of BBR remains substantially constrained by its poor oral bioavailability, rapid systemic metabolism, and lack of effective kidney-specific accumulation [27, 28]. Furthermore, its toxicity is route-dependent; while intraperitoneal and intravenous administration exhibit relatively median lethal dose (LD50) in mice, intragastric administration shows no obvious toxicity, confining its safe use primarily to the oral route [29]. Therefore, developing strategies to overcome these pharmacokinetic and targeting limitations is both necessary and of considerable clinical significance. Nanotechnology-based delivery systems have been proposed as a viable solution, as nanoparticle encapsulation of BBR can enhance its stability, prolong circulation time, and allow co-delivery or surface assembly of additional therapeutic agents [30–32]. By encapsulating BBR within nanocarriers, it is possible to shield the drug from premature degradation, prolong its systemic circulation, and facilitate targeted delivery to the site of injury, thereby maximizing therapeutic index while minimizing off-target effects [33–35].

Among various delivery platforms, zeolitic imidazolate frameworks (ZIFs) have emerged as attractive carriers for drug delivery because of their highly ordered porous architecture, large surface area, tunable composition, and favorable loading capacity for small-molecule therapeutics such as BBR [36–39]. Recent studies have further highlighted the versatility of ZIF-based systems in improving cargo protection, microenvironment responsiveness, and therapeutic performance, supporting their growing use in advanced biomedical delivery platforms [40–43]. More importantly, the coordination between zinc ions and imidazole ligands can provide a protective framework that helps shield encapsulated drugs from premature degradation or loss of activity during delivery [44–46]. However, because ZIFs are relatively acid-sensitive, oral administration generally requires additional surface protection to reduce gastric erosion, preserve nanoparticle integrity, and maintain downstream drug bioavailability [47–50]. This consideration is particularly important because orally administered nanoparticles must first pass through the acidic gastric environment before intestinal absorption, and insufficient stability at this stage may lead to premature carrier disruption and drug leakage. To address this limitation, we introduced an epigallocatechin gallate (EGCG)-based shell onto the particle surface [51–55]. As a natural polyphenol, EGCG possesses potent antioxidant activity and excellent interfacial versatility, and polyphenol-based materials have been increasingly explored in biomedical systems because they can simultaneously provide structural stabilization and bioactive microenvironment modulation [56–60]. In addition to its capacity to scavenge reactive oxygen species (ROS), EGCG may synergize with the pharmacological actions of BBR, while also stabilizing the nanoparticle surface and improving resistance of the ZIF core to the harsh gastric environment during oral administration [47, 61]. Therefore, the combination of a ZIF core and an EGCG shell provides a rational oral nanoplatform for improving the stability, delivery efficiency, and therapeutic efficacy of BBR in diabetic kidney disease.

Guided by this rationale, we developed a novel polyphenol-modified nanosystem, ZIF-BBR-BPNs, specifically designed to amplify the renoprotective potential of berberine in the treatment of DKD (Fig. 1). To systematically assess the therapeutic efficacy and underlying mechanisms of this platform, we first characterized the structural integrity and protective shielding effects conferred by the EGCG-coated ZIF core. Subsequently, *in vitro* studies were conducted using glomerular endothelial cells to investigate whether the synergistic combination of BBR and EGCG could effectively mitigate oxidative stress and restore endothelial function. To further validate its clinical relevance, we employed the db/db mouse model to assess the systemic pharmacokinetic advantages and the targeted renal accumulation of ZIF-BBR-BPNs. Specifically, we focused on its capacity to alleviate hallmark DKD pathologies, including albuminuria, glomerular basement membrane thickening, and chronic inflammation. By comparing its performance with free BBR and clinical metformin, this study aims to establish whether this multi-targeted nanoparticle strategy can overcome the pharmacological bottlenecks of BBR and provide a superior therapeutic outcome for DKD.

2 Experimental

2.1 Materials

BBR, 2-methylimidazole (2-MIM, 99%), zinc nitrate hexahydrate ($ZnNO_3{\cdot}6H_2O$, 99%), methanol (CH_3OH, 99.9%), and Cy5-Amine chloride hydrochloride (Cy5) were purchased from Aladdin Biochemical Technology Co., Ltd. (Shanghai, China). EGCG (98%) was sourced from DASF Bio-Technology Co., Ltd. (Nanjing, China). 1,4-Phenylenediboronic acid (BA, 98%), 1,1-diphenyl-2-

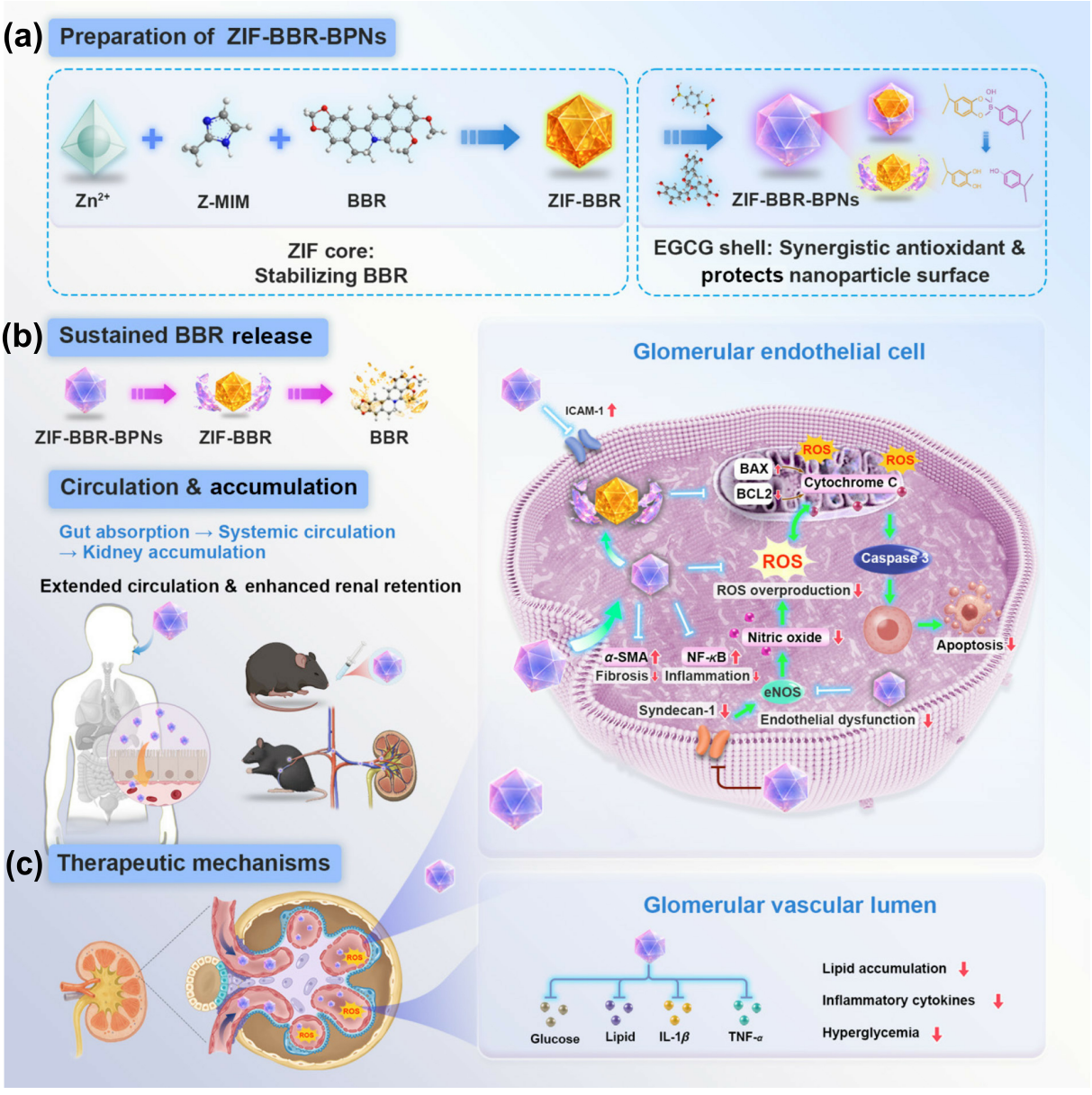

Figure 1 Schematic of ZIF-BBR-BPNs construction, preparation, and multi-targeted therapeutic mechanism of ZIF-BBR-BPNs for DKD therapy. (a) Engineering of ZIF-BBR-BPNs featuring a ZIF core for BBR encapsulation and an EGCG-based metal-phenolic network coating. (b) Systemic administration, prolonged circulation, and passive targeted accumulation of ZIF-BBR-BPNs in the injured kidney. (c) The multi-targeted therapeutic effects of the nanoplatform, including systemic metabolic regulation (hypoglycemic and lipid-lowering) and direct renal cell protection through anti-inflammatory, anti-fibrotic, and anti-apoptotic pathways.

picrylhydrazyl (DPPH, 97%), 2,2'-azino-bis(3-ethylbenzothiazoline-6-sulfonic acid) (ABTS, 98%) were acquired from Energy Chemical (Anhui, China).

2.2 Animals

Male db/m mice (C57BL/6J background) and db/db mice (leptin receptor-deficient, DKD model) were purchased from Cyagen Biosciences. Mice were housed in a specific pathogen-free (SPF) environment with a 12 h light/12 h dark cycle schedule at 22 ± 2 °C, and free access to food and water. All animal experiments were approved by the Institutional Animal Care and Use Committee of West China Hospital, Sichuan University (Approval No. 20250808006) and were performed in accordance with the Guide for the Care and Use of Laboratory Animals.

2.3 Preparation of ZIF-BBR-BPNs

ZIF-BBR was first synthesized following a standard metal-organic framework assembly protocol, after which a BPNs coating was introduced through the co-coordination of EGCG and BA on the particle surface. Specifically, 2-MIM (20 mmol) and BBR (200 mmol) were dissolved in methanol (100 mL), while $ZnNO_3{\cdot}6H_2O$ (10 mmol) was separately dissolved in an additional 100 mL of methanol. The two solutions were combined and allowed to stand at 25 °C for 12 h, yielding a yellow precipitate. The resulting solid was collected by centrifugation, washed repeatedly with methanol, and freeze-dried to obtain ZIF-BBR. Then 10-mL dispersion of ZIF-BBR (1 mg/mL) was prepared for subsequent coating. In parallel, EGCG (80 mg) and BA (29 mg) were dissolved in 40 mL of methanol. This solution was added dropwise to the ZIF-

BBR dispersion under continuous stirring and allowed to react at room temperature for 12 h, producing a black precipitate. The final product was isolated by centrifugation, washed three times with methanol, and dried to afford ZIF-BBR-BPNs.

2.4 Characterization of ZIF-BBR-BPNs

The surface morphologies of ZIF-BBR-BPNs were acquired on Nova Nano scanning electron microscopy (SEM) 450 microscope and transmission electron microscopy (TEM, Talos F200i, Thermo Scientific), and the elemental mapping of B, N, O, Zn, and C in specific sample regions was collected using the energy dispersive spectroscopy (EDS) attached to the TEM. Dynamic light scattering (DLS) and zeta potential measurements were characterized by a Malvern Zetasizer Nano ZS particle analyzer. Fourier-transform infrared spectroscopy (FT-IR) spectra were performed with PerkinElmer spectrum one B system using KBr pellets methods with the resolution of 4.0 cm^{-1}. X-ray photoelectron spectroscopy (XPS) measurements were performed with a VG ESCALAB MKII spectrometer. XPSPEAK software (version 4.1) was used to deconvolute the wide-scan and narrow-scan XPS spectra of Zn 2p, B 1s, C 1s, O 1s, and N 1s.

2.5 *In vitro* release behavior of ZIF-BBR-BPNs

The release of BBR from ZIF-BBR-BPNs was evaluated in simulated gastric fluid (SGF) and phosphate-buffered saline (PBS). A standard calibration curve was generated by recording the absorbance of BBR at 350 nm with a microplate reader across a series of known concentrations. For release assays, dispersions of ZIF-BBR-BPNs were loaded into dialysis bags (molecular weight cut-off: 500 Da) and immersed separately in SGF and PBS. Samples of the external medium were collected at 1 h intervals during the initial phase and at 5 h intervals thereafter, and the absorbance was measured at 350 nm. BBR concentrations and cumulative release profiles were calculated using the established calibration curve.

2.6 *In vitro* antioxidant assessment of ZIF-BBR-BPNs

The radical-scavenging capacities of ZIF-BBR and ZIF-BBR-BPNs were assessed using DPPH and ABTS assays in ethanol and aqueous media, respectively. Fresh DPPH solution in ethanol (1.0×10^{-3} M) and ABTS solution in water (7.0×10^{-3} M) were prepared prior to testing. For the DPPH assay, samples (ZIF-BBR or ZIF-BBR-BPNs) were mixed with 300 μL of DPPH solution and brought to a final volume of 3.0 mL with ethanol. After mixing, absorbance at 517 nm was recorded at indicated time points up to 30 min. For the ABTS assay, 100 μL of ABTS radical cation solution was combined with the prepared samples and diluted to 3.0 mL with deionized water (2900 μL). The absorbance at 714 nm was then monitored at indicated incubation times up to 30 min.

2.7 *In vitro* cell experiments

Human renal glomerular endothelial cells (HRGECs) were cultured in Dulbecco's modified Eagle medium (DMEM) supplemented with 10% fetal bovine serum (FBS) and 1% Penicillin-Streptomycin at 37 °C in a 5% CO_2 incubator. For high glucose and high cholesterol (HG+HC)-induced injury, cells were treated with DMEM containing 25 mM glucose + 100 μg/mL cholesterol for 48 h. Compared with high glucose alone, the HG+HC condition was used to better mimic the glucolipotoxic microenvironment of DKD, in which hyperglycemia is accompanied by lipid metabolic stress. For H_2O_2-induced injury, cells were treated with 800 μM H_2O_2 for 24 h. Cells were divided into groups: (1) normal control (NG: 5.5 mM glucose); (2) injury model (HG+HC or H_2O_2); (3) BBR low dose (30 μM); (4) BBR high dose (90 μM); (5) ZIF-BBR-BPNs low dose (30 μM equivalent BBR); (6) ZIF-BBR-BPNs high dose (90 μM equivalent BBR).

2.8 Cell viability assay

Cells were plated in 96-well plates and exposed to the indicated treatments. Cell viability was quantified using a Cell Counting Kit-8 (CCK-8) kit following the supplier's protocol.

2.9 Apoptosis detection

Cells were seeded in 6-well plates and treated as described above. After treatment, cells were collected, rinsed with PBS, and stained with Annexin V-FITC and propidium iodide (PI) for 15 min at room temperature in the dark. Apoptotic cells were analyzed by flow cytometry (Beckman CytoFLEX).

2.10 ROS detection

Cells were seeded in 6-well plates and treated as described above. The 2',7'-dichlorodihydrofluorescein diacetate (DCFH-DA) probe was then added, and the cells were incubated at 37 °C for 30 min. Fluorescence signals were subsequently captured using a fluorescence microscope (Leica DMI8, Wetzlar, Germany).

2.11 *In vivo* efficacy assessment in db/db mice

Nine-week-old db/db mice were randomly divided into 4 groups (n = 6 per group): (1) db/db vehicle group (gavaged with normal saline); (2) BBR group (gavaged with free BBR, 150 mg/kg); (3) ZIF-BBR-BPNs group (gavaged with ZIF-BBR-BPNs, 150 mg/kg equivalent BBR); (4) metformin group (gavaged with metformin, 150 mg/kg). Age-matched db/m mice (n = 6) served as the normal control group. All treatments were administered for 4 weeks.

2.12 General physiological indicators

Body weight: The body weight of each mouse was measured weekly using an electronic balance. Measurements were taken at the same time of day (morning) to minimize diurnal variation. Fasting blood glucose (FBG): Mice were fasted for 6 h before blood collection. Blood samples were collected from the tail vein, and glucose levels were measured using a calibrated glucometer (e.g., Accu-Chek, Roche). Measurements were performed weekly, at the same time of day for consistency.

2.13 Renal function assessment

Urine samples were collected at the end of the treatment. Urine albumin concentration was measured by enzyme-linked immunosorbent assay (ELISA), and urine creatinine concentration was determined using a creatinine assay kit (Shanghai ZCIBIO Technology Co., Ltd.). Urine albumin/creatinine ratio (UACR) was calculated as the ratio of urine albumin to urine creatinine.

Inflammatory cytokine detection: The levels of tumor necrosis factor-alpha (TNF-α) and interleukin-1 beta (IL-1β) in serum were measured using ELISA kits according to the manufacturer's instructions.

Histopathological analysis: Renal tissues were fixed in 4% paraformaldehyde for 24 h, embedded in paraffin, and cut into 4 μm sections. Sections were stained with hematoxylin-eosin (H&E), periodic acid-Schiff (PAS), and Masson's trichrome, respectively. H&E staining was used to observe glomerular

structure; PAS staining was used to evaluate mesangial matrix expansion; Masson staining was used to assess renal interstitial fibrosis. For transmission electron microscopy (TEM), renal cortex samples were fixed in 2.5% glutaraldehyde, embedded in epoxy resin, cut into ultra-thin sections (50 nm), stained with uranyl acetate and lead citrate, and observed using a TEM (JEM-2100).

In vivo distribution of ZIF-BBR-BPNs: Cy5-labeled ZIF-BBR-BPNs were obtained by introducing Cy5 during the post-synthetic modification process. Specifically, 2 mL of a 1 mg/mL Cy5 solution was added to 10 mL of the prepared 1 mg/mL ZIF-BBR-BPNs dispersion. The mixture was stirred for 24 h to allow efficient conjugation, followed by centrifugation and repeated washing to yield the purified Cy5-labeled ZIF-BBR-BPNs. Eight-week-old db/m and db/db mice (n = 3 per group) were orally gavaged with Cy5-labeled ZIF-BBR-BPNs (150 mg/kg equivalent BBR). *In vivo* fluorescence imaging was performed at 0.5, 1, 2, 6, 12, and 24 h post-administration using Bruker Spectral Instruments Imaging (Bruker SII). At 6, 12 and 24 h post-administration, mice were euthanized, and major organs (kidney, liver, spleen, heart, lung and pancreas) were harvested. *Ex vivo* fluorescence intensity of each organ was measured using the same imaging system.

2.14 Measurement of berberine concentration

BBR concentration was quantified using a competitive ELISA kit (PK186243-96T, Shanghai Bohu Biotechnology Co., Ltd.) following the manufacturer's instructions. Samples and standards were incubated in anti-BBR antibody-coated plates together with horseradish peroxidase (HRP)-labeled antigen, and absorbance was read at 450 nm.

2.15 Immunohistochemistry

Paraffin-embedded sections were deparaffinized and rehydrated, followed by antigen retrieval. Sections were incubated with primary antibodies at 4 °C overnight: anti-F4/80 (1:600, Proteintech, Chicago, USA), anti-ICAM-1 (1:300, Abiowell, Wuhan, China), anti-Collagen IV (1:200, Thermo Fisher Scientific, Waltham, USA), and anti-α-SMA (1:400, Boster, Wuhan, China). Then sections were incubated with an HRP-conjugated secondary antibody (1:500) for 1 h at room temperature. Diaminobenzidine (DAB) was used for color development, and hematoxylin was applied for counterstaining.

2.16 Western blot analysis

Cells or renal tissues were lysed in radioimmunoprecipitation assay (RIPA) lysis buffer supplemented with protease and phosphatase inhibitors. Protein concentration was determined using a bicinchoninic acid (BCA) protein assay kit. Equal amounts of protein were separated by 10% SDS-PAGE and transferred to polyvinylidene fluoride (PVDF) membranes. After blocking with 5% non-fat milk for 1 h at room temperature, the membranes were incubated overnight at 4 °C with the following primary antibodies: anti-eNOS (1:1000, Abclonal, Wuhan, China); anti-p-eNOS (1:1000, Abclonal, Wuhan, China); anti-Syndecan-1 (1:500, Huaan, Hangzhou, China); anti-BAX (1:1000, Proteintech, Wuhan, China); anti-BCL2 (1:1000, Proteintech, Wuhan, China); anti-Caspase-3 (1:500, Huaan, Hangzhou, China); anti-Active Caspase-3 (1:500, Huaan, Hangzhou, China); and anti-β-tubulin (1:5000, ZSGB-BIO, Beijing, China). After washing, membranes were incubated with an HRP-labeled secondary antibody (1:5000) for 1 h at room temperature. Signals were developed using an enhanced chemiluminescence (ECL) substrate, and band densities were quantified in ImageJ (NIH, Bethesda, MD, USA) with β-tubulin as the loading control.

2.17 Statistical analysis

All data were expressed as mean ± standard deviation (SD). Statistical analysis was performed using GraphPad Prism 10.0 software (GraphPad Software, San Diego, CA, USA). Differences between groups were analyzed using one-way analysis of variance (ANOVA) followed by Tukey's post-hoc test. $P < 0.05$ was considered statistically significant.

3 Results and discussion

3.1 Preparation and characterization of ZIF-BBR-BPNs

ZIF-BBR was synthesized by encapsulating BBR using a conventional metal-organic framework strategy with 2-MIM and $ZnNO_3{\cdot}6H_2O$, followed by surface coating with EGCG and p-phenyldiboronic acid (BA) to obtain ZIF-BBR-BPNs (Fig. 2(a)). Comprehensive characterization confirmed the successful preparation of both components. SEM revealed that ZIF-BBR and ZIF-BBR-BPNs exhibited well-defined rhombic dodecahedral morphologies (Fig. 2(b) and Fig. S1 in the Electronic Supplementary Material (ESM)). DLS measurements indicated uniform particle sizes for both ZIF-BBR and ZIF-BBR-BPNs, approximately 150 nm, with a slight increase after BPNs coating, consistent with successful surface modification (Fig. 2(c)). Zeta potential analysis showed that ZIF-BBR-BPNs had a surface potential of approximately −10 mV, attributed to the ionizable phenolic hydroxyl and boronic acid groups of the BPNs coating (Fig. 2(d)), suggesting good colloidal stability, favorable for long-term storage and subsequent biological applications. Transmission electron microscopy (TEM) further confirmed the morphology and size of ZIF-BBR-BPNs, showing a BPNs coating thickness of ~ 5 nm (Fig. 2(e) and Fig. S2 in the ESM). Elemental mapping by TEM revealed the presence of B, N, O, Zn, and C elements in ZIF-BBR-BPNs, confirming both successful BBR encapsulation within the ZIF-8 framework and effective BPNs surface modification (Fig. 2(f)). Additionally, quantitative analysis revealed a BBR loading content of 27% in the ZIF-BBR-BPNs, indicating their strong potential for efficient drug delivery (Fig. 2(g)). Because oral nanoplatforms must first withstand the acidic gastric environment before intestinal absorption, we next evaluated the stability and release behavior of ZIF-BBR-BPNs in SGF and PBS. As shown in the release profiles calculated from a standard calibration curve, the BBR release rate was moderately enhanced under acidic conditions compared with neutral conditions (Fig. 2(h) and Fig. S3 in the ESM). After 24 h, approximately 37% of BBR was released at SGF, whereas ~ 29% was released at PBS, indicating an overall slow and sustained release. Notably, although an initial release occurred under acidic conditions, a substantial amount of BBR remained protected within the ZIF matrix, ensuring sufficient drug availability for subsequent therapeutic action.

Then, Fourier-transform infrared (FTIR) spectroscopy displayed strong hydroxyl peaks around ~ 3500 cm^{-1} and pronounced carbonyl peaks at ~ 1600 cm^{-1} in ZIF-BBR-BPNs, indicative of successful BBR loading and BPNs coating (Fig. 2(i) and Fig. S4 in the ESM). XPS wide-scan spectra revealed characteristic core-level peaks of Zn 2p, B 1s, O 1s, C 1s, and N 1s in ZIF-BBR-BPNs,

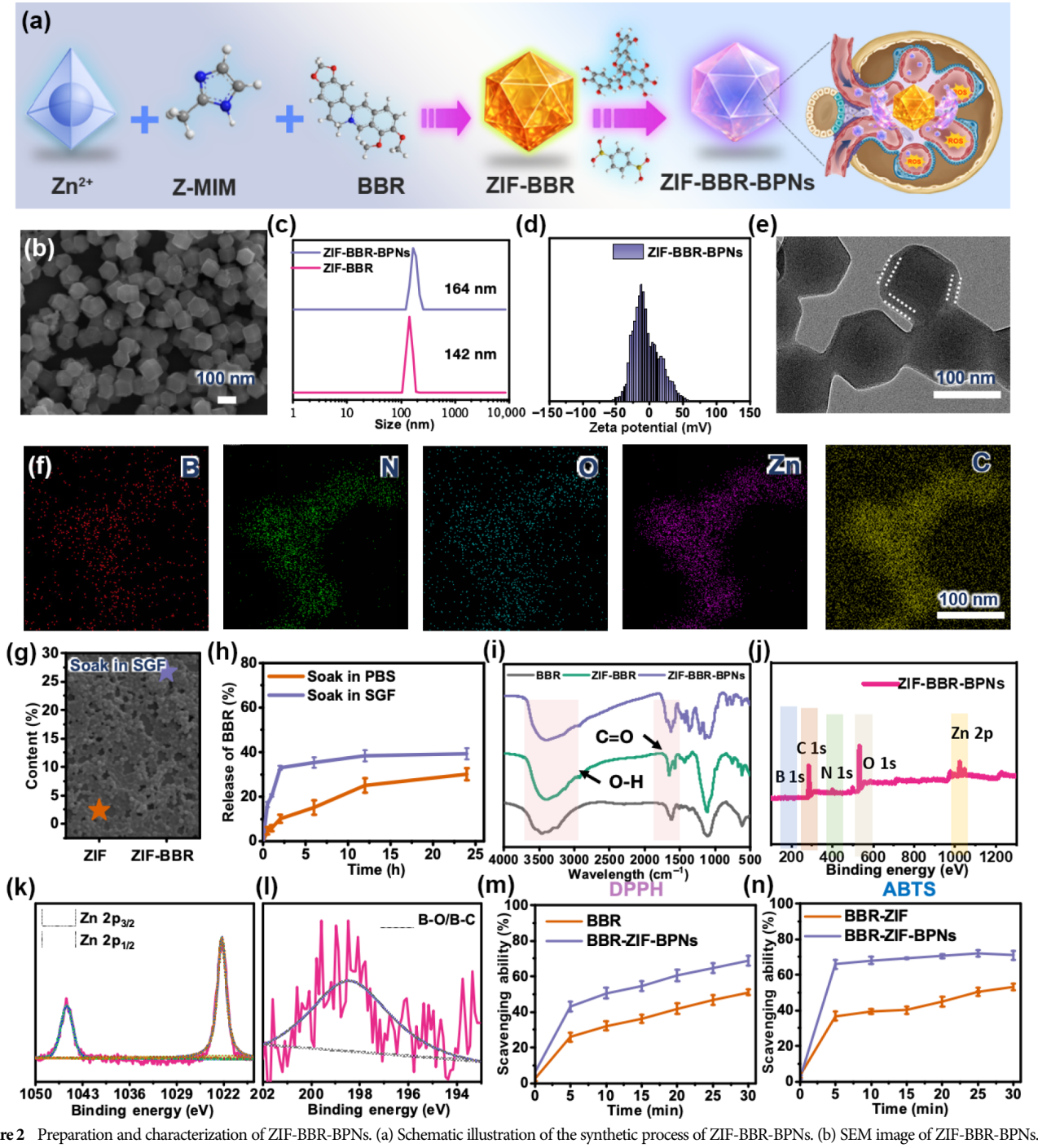

Figure 2 Preparation and characterization of ZIF-BBR-BPNs. (a) Schematic illustration of the synthetic process of ZIF-BBR-BPNs. (b) SEM image of ZIF-BBR-BPNs. (c) DLS size distributions of ZIF-BBR and ZIF-BBR-BPNs. (d) Zeta potential analysis of ZIF-BBR-BPNs. (e) TEM image and (f) elemental mapping of ZIF-BBR-BPNs. (g) Drug-loading content of ZIF-BBR and SEM image of ZIF-BBR-BPNs after soaking in SGF. (h) Release of BBR after soaking in SGF and PBS. (i) FTIR spectra of BBR, ZIF-BBR, and ZIF-BBR-BPNs. (j) XPS wide-scan spectrum of ZIF-BBR-BPNs. (k) Zn 2p and (l) B 1s high-resolution XPS spectra of ZIF-BBR-BPNs. (m) DPPH and (n) ABTS radical-scavenging activities of ZIF-BBR-BPNs.

derived from both ZIF-BBR and the EGCG/BA coating (Fig. 2(j) and Fig. S5 in the ESM). High-resolution Zn 2p spectra confirmed the integrity of the ZIF-8 framework (Fig. 2(k)), while B 1s spectra verified the presence of dynamic boronate ester bonds between EGCG and BA, demonstrating the successful formation of the BPNs coating (Fig. 2(l)). The antioxidant activity of ZIF-BBR and ZIF-BBR-BPNs was further evaluated using DPPH and ABTS radical scavenging assays. As shown in Figs. 2(m)–2(n), the scavenging capacity of both nanoparticles increased over time. For example, at 30 min, the DPPH scavenging ability reached ~ 50% for ZIF-BBR and ~ 70% for ZIF-BBR-BPNs. The enhanced antioxidant activity after BPNs coating is attributed to the superior ROS-scavenging capability of EGCG. Overall, these results demonstrate the successful fabrication of BBR-loaded ZIF-BBR nanoparticles with a functional BPNs coating. The resulting ZIF-BBR-BPNs exhibit efficient drug loading and controlled release, along with

excellent radical scavenging activity, providing a robust foundation for subsequent *in vivo* applications.

3.2 ZIF-BBR-BPNs protect glomerular endothelial cells from DKD injury

Cell viability assays showed that ZIF-BBR-BPNs (dosed at BBR-equivalent concentrations) were non-toxic to HRGECs at physiological doses, whereas higher concentrations reduced viability (Fig. 3(a)), indicating a favorable therapeutic window for ZIF-BBR-BPNs. H_2O_2 exposure decreased HRGEC viability in a concentration-dependent manner (Fig. 3(b)). Critically, in H_2O_2-injured HRGECs, ZIF-BBR-BPNs restored viability dose-dependently: 50 μM ZIF-BBR-BPNs rescued viability from ~ 50% (H_2O_2-only control) to nearly 100% (Fig. 3(c)), confirming efficacy against oxidative stress-mediated endothelial damage. Consistently, flow cytometry (Fig. 3(d)) and its quantification (Fig. S6 in the ESM) showed that H_2O_2 markedly increased HRGEC apoptosis, which was dose-dependently attenuated by BBR, with ZIF-BBR-BPNs exhibiting superior anti-apoptotic efficacy.

The antioxidant effects of ZIF-BBR-BPNs were further

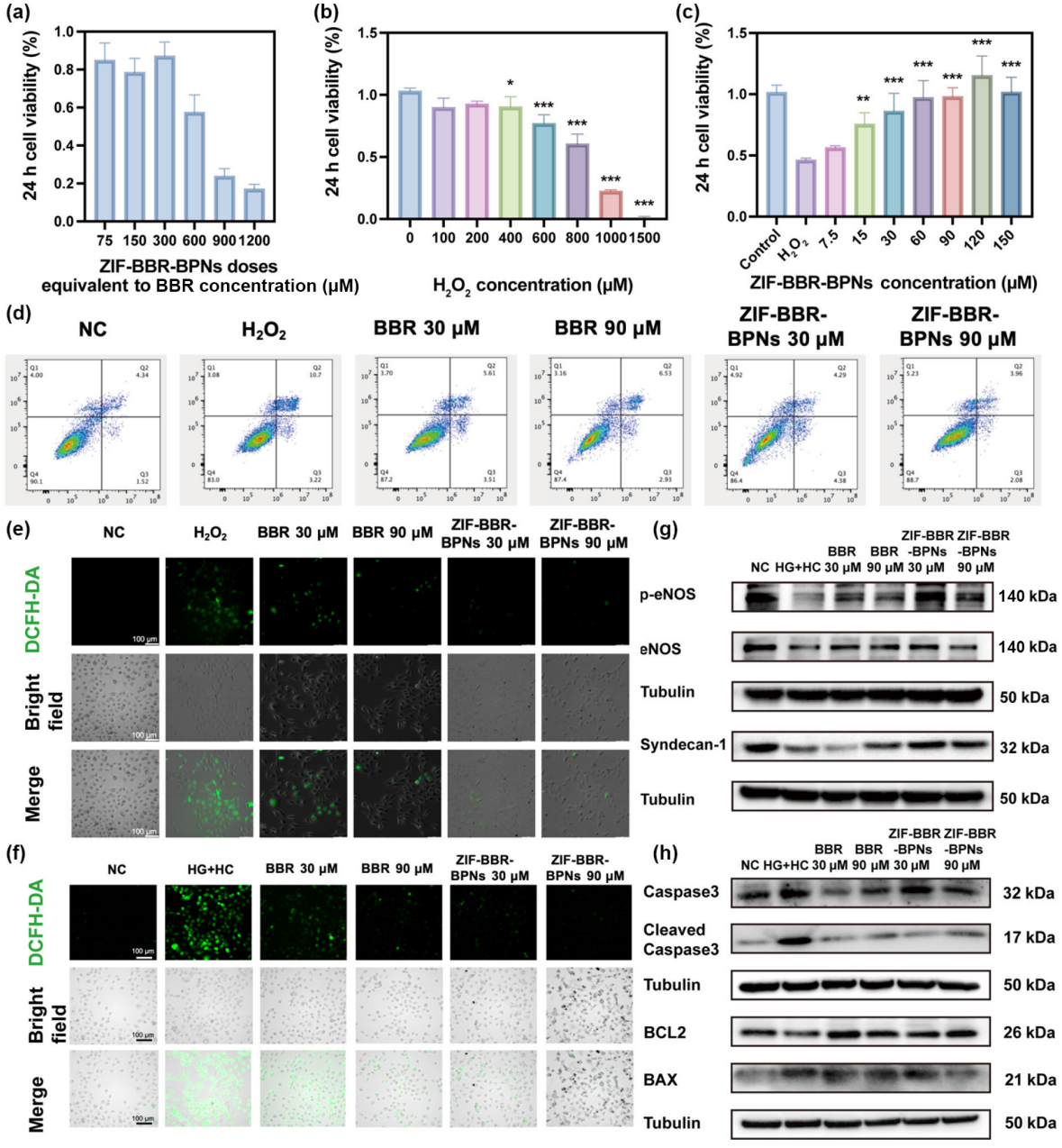

Figure 3 ZIF-BBR-BPNs protect HRGECs in DKD-like injury models. (a) HRGEC viability at 24 h after ZIF-BBR-BPNs treatment (BBR-equivalent, μM). (b) HRGEC viability at 24 h after H_2O_2 exposure (μM). (c) HRGEC viability at 24 h in Control, H_2O_2, and H_2O_2 + ZIF-BBR-BPNs (μM). (d) Representative flow cytometry plots of apoptosis under H_2O_2 with NC (negative control), H_2O_2, free BBR (30/90 μM), or ZIF-BBR-BPNs (30/90 μM). (e) Representative ROS images (DCFH-DA, bright field, merge) under H_2O_2 (4 h) with the indicated treatments (scale bars: 100 μm). (f) Representative ROS images (DCFH-DA, bright field, merge) under HG+HC (high glucose and high cholesterol) with the indicated treatments (scale bars: 100 μm). (g) Representative Western blots of p-eNOS, eNOS, and Syndecan-1 under HG+HC (*β*-tubulin loading control). (h) Representative Western blots of apoptosis proteins (Caspase-3, Cleaved Caspase-3, BCL2, BAX) under HG+HC (*β*-tubulin loading control). Data are presented as mean ± SD. In panel (b), $^*P < 0.05$ and $^{***}P < 0.001$ vs. the 0 μM H_2O_2 group. In panel (c), $^{**}P < 0.01$ and $^{***}P < 0.001$ vs. the H_2O_2 group.

confirmed by intracellular ROS measurements. Both H_2O_2 and HG+HC stimulation robustly elevated ROS levels in HRGECs (Figs. 3(e) and 3(f)), whereas ZIF-BBR-BPNs significantly reduced ROS fluorescence intensity in both models, indicating potent ROS-scavenging activity. Given the central role of oxidative stress in DKD progression, this strong antioxidant capacity provides a key basis for the multi-target therapeutic actions of ZIF-BBR-BPNs. At the molecular level, Western blot analysis under HG+HC conditions showed that HG+HC downregulated phosphorylated eNOS, total eNOS, and the endothelial marker Syndecan-1 (Fig. 3(g)), while ZIF-BBR-BPNs effectively restored their expression, as confirmed by quantitative analysis (Fig. S7 in the ESM), suggesting preservation of endothelial function via activation of eNOS signaling and maintenance of the glomerular filtration barrier.

Furthermore, HG+HC induced a pro-apoptotic shift in apoptosis-related proteins, characterized by increased Cleaved Caspase3 and BAX, and decreased BCL2 (Fig. 3(h)). ZIF-BBR-BPNs reversed these alterations, inhibiting caspase activation and rebalancing the BCL2/BAX ratio, thereby suppressing mitochondrial pathway-mediated apoptosis. Collectively, these *in vitro* data demonstrate that ZIF-BBR-BPNs protect HRGECs from DKD-related injury through a coordinated strategy of enhancing cell viability, mitigating oxidative stress, inhibiting apoptosis, and activating eNOS signaling to preserve endothelial function, thus providing comprehensive cytoprotection against glomerular endothelial injury in DKD.

3.3 ZIF-BBR-BPNs improve systemic and renal outcomes in DKD mice

To evaluate the therapeutic efficacy of ZIF-BBR-BPNs, db/db (DKD model) and db/m (control) mice underwent a 4-week treatment regimen, as outlined in Fig. 4(a). Metabolic profiling revealed that db/db mice had significantly higher body weight than db/m controls; however, no significant weight differences were observed among the db/db treatment groups during the intervention (Fig. 4(b)). As expected, db/db mice exhibited marked hyperglycemia, but elevated fasting blood glucose levels were significantly reduced by treatment with BBR, ZIF-BBR-BPNs, or metformin (Figs. 4(c) and 4(d)). Dyslipidemia in db/db mice, characterized by increased serum triglycerides, total cholesterol, and LDL-cholesterol, showed a trend toward improvement in all treatment groups, although these changes did not reach statistical significance (Figs. S8(a)–S8(c) in the ESM).

Notably, ZIF-BBR-BPNs provided more pronounced renoprotection than free BBR or metformin when renal injury was assessed. uACR was dramatically elevated in db/db mice, but all treatments reduced this elevation. Importantly, ZIF-BBR-BPNs achieved the largest decline, corresponding to approximately a 40% reduction relative to the db/db group (Fig. 4(e)). Although serum creatinine remained unchanged (Fig. 4(f)), blood urea nitrogen (BUN) and the sensitive renal injury marker serum cystatin C (Cys-C) were significantly elevated in db/db mice, but were notably reversed by BBR and ZIF-BBR-BPNs (Figs. 4(g) and 4(h)). In parallel, serum levels of the pro-inflammatory cytokines TNF-α and IL-1β, which were significantly elevated in db/db mice, were effectively reduced by ZIF-BBR-BPNs, BBR, and metformin, with ZIF-BBR-BPNs showing particularly strong anti-inflammatory activity (Figs. 4(i) and 4(j)).

A key pathological feature of DKD, glomerular basement membrane (GBM) thickening, was evident in db/db mice and was significantly attenuated by all treatments, particularly by ZIF-BBR-BPNs and BBR (Fig. 4(k)). Consistent with this, histopathological and ultrastructural analyses revealed pronounced renal injury, collagen deposition, and glomerular lesions in db/db mice, as observed in H&E, Masson trichrome, and PAS staining. These signs of renal damage were markedly ameliorated following treatment, with ZIF-BBR-BPNs conferring the most robust structural protection (Fig. 4(l)).

3.4 Enhanced systemic exposure and passive renal accumulation of ZIF-BBR-BPNs *in vivo*

Having demonstrated that ZIF-BBR-BPNs markedly ameliorate metabolic abnormalities and renal injury in db/db mice, we next examined their *in vivo* distribution to gain insight into the mechanisms underlying the enhanced therapeutic efficacy. Whole-body and organ/tissue fluorescence imaging was performed in Control and DKD mice following oral administration of Cy5-labeled ZIF-BBR-BPNs. *In vivo* fluorescence imaging showed stronger and more sustained Cy5 signals in DKD mice compared with Control mice over time, with detectable fluorescence persisting up to 12 h after oral gavage (Fig. 5(a)). *Ex vivo* fluorescence imaging of major organs harvested at 6, 12, and 24 h further confirmed significantly higher fluorescence intensity in the kidneys of DKD mice (Fig. 5(b)). Consistently, fluorescence imaging of kidney sections revealed pronounced Cy5 signal accumulation in DKD renal tissues, whereas only weak signals were observed in Control mice (Fig. 5(c)). This enhanced renal exposure is consistent with the superior renoprotective outcomes observed *in vivo* and suggests that disease-associated physiological alterations may favor renal deposition of the nanoformulation. In DKD, glomerular barrier injury, including endothelial glycocalyx damage, GBM remodeling, and increased vascular permeability, may facilitate nanoparticle access to injured renal tissue. In addition, the inflammatory renal microenvironment may promote an enhanced permeability and retention (EPR)-like retention effect, thereby favoring prolonged intrarenal localization of circulating nanocarriers. Altered interactions with renal uptake pathways may also contribute to this process.

To further elucidate the basis for this distribution pattern, serum concentration-time profiles of BBR were evaluated following oral administration of free BBR and ZIF-BBR-BPNs (Fig. 5(d)). ZIF-BBR-BPNs exhibited markedly increased circulating BBR levels over time compared with free BBR, indicating improved oral bioavailability and prolonged systemic exposure. The observed enhancement in plasma exposure can be attributed to the improved pharmacokinetic properties conferred by the ZIF-based nanoformulation. Encapsulation of BBR within the ZIF framework, together with the EGCG coating, enhances drug stability during gastrointestinal transit and systemic circulation, thereby reducing premature degradation and clearance. The resulting elevation in systemic availability facilitates passive accumulation of BBR in highly perfused and injury-prone organs such as the kidney, which may be sufficient to amplify its therapeutic action under diabetic conditions without the need for active targeting mechanisms.

Notably, enhanced plasma exposure and sustained renal presence of ZIF-BBR-BPNs provide a plausible explanation for their superior efficacy in reducing albuminuria, inflammation, and structural renal damage compared with free BBR. This

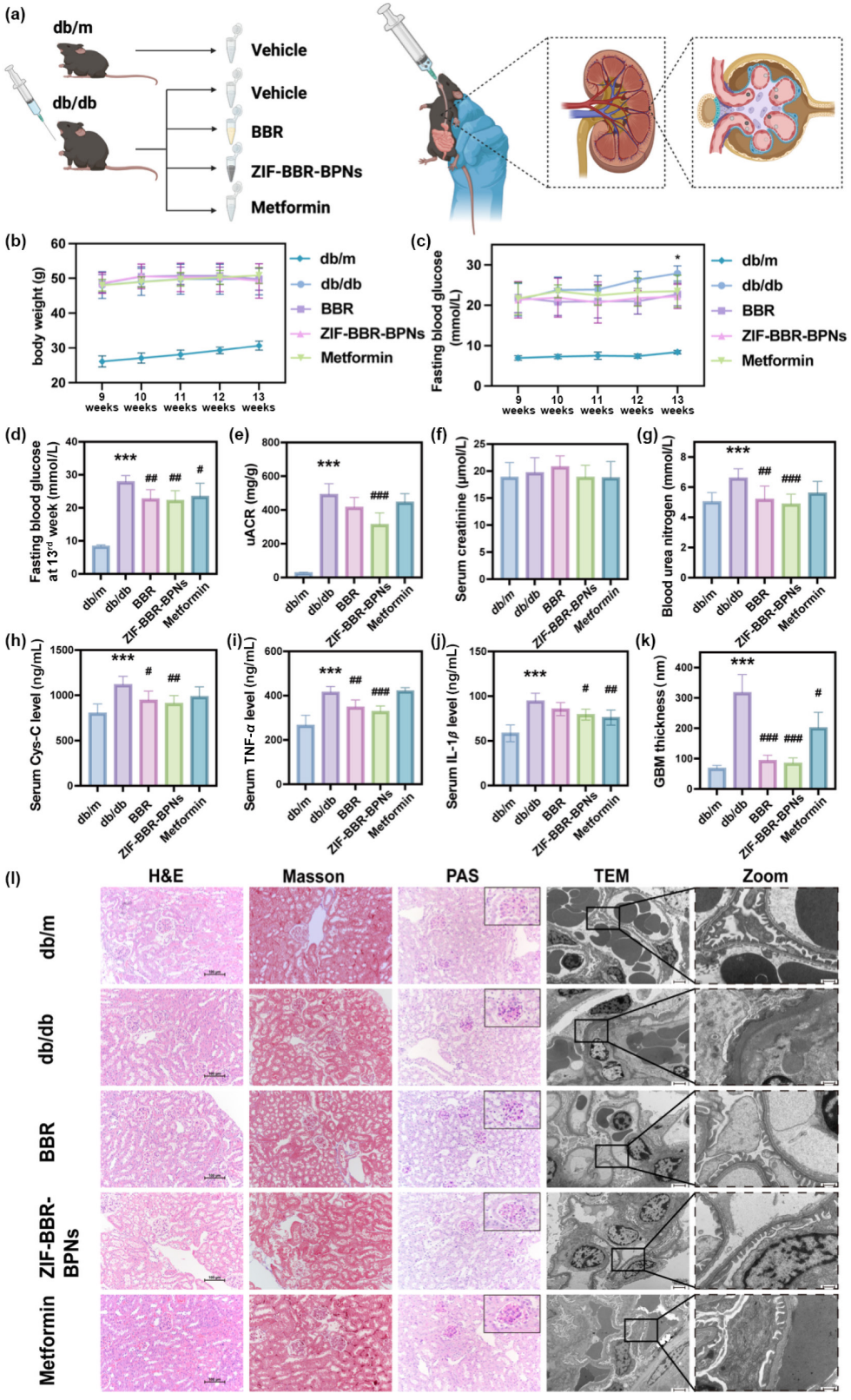

Figure 4 ZIF-BBR-BPNs ameliorate metabolic and renal injury in db/db DKD mice. (a) Schematic of the experimental design. Db/m (control) and db/db (DKD) mice received daily oral gavage of vehicle, BBR, ZIF-BBR-BPNs, or metformin for 4 weeks (n = 6). The kidney and glomerulus (therapeutic target) are illustrated on the right. (b) Time-course changes in body weight and (c) fasting blood glucose from 9 to 13 weeks of age. Endpoint metabolic and renal injury indices, including (d) fasting blood glucose at the 13th week, (e) urinary albumin-to-creatinine ratio (uACR), (f) serum creatinine, (g) BUN, (h) serum cystatin C (Cys-C), (i) serum TNF-α, (j) serum IL-1β, and (k) GBM thickness. (l) Representative renal histopathological staining and ultrastructural images, including H&E staining, Masson's trichrome staining, PAS staining, and TEM. The boxed areas in the PAS and TEM panels indicate the magnified regions. Scale bars: 100 μm for H&E, Masson, and PAS; 2 μm and 500 nm (zoomed) for TEM. Data in panels (d)–(k) are presented as mean ± SD. $^{*}P < 0.05$ and $^{***}P < 0.001$ vs. db/m group; $^{\#}P < 0.05$, $^{\#\#}P < 0.01$, and $^{\#\#\#}P < 0.001$ vs. db/db group.

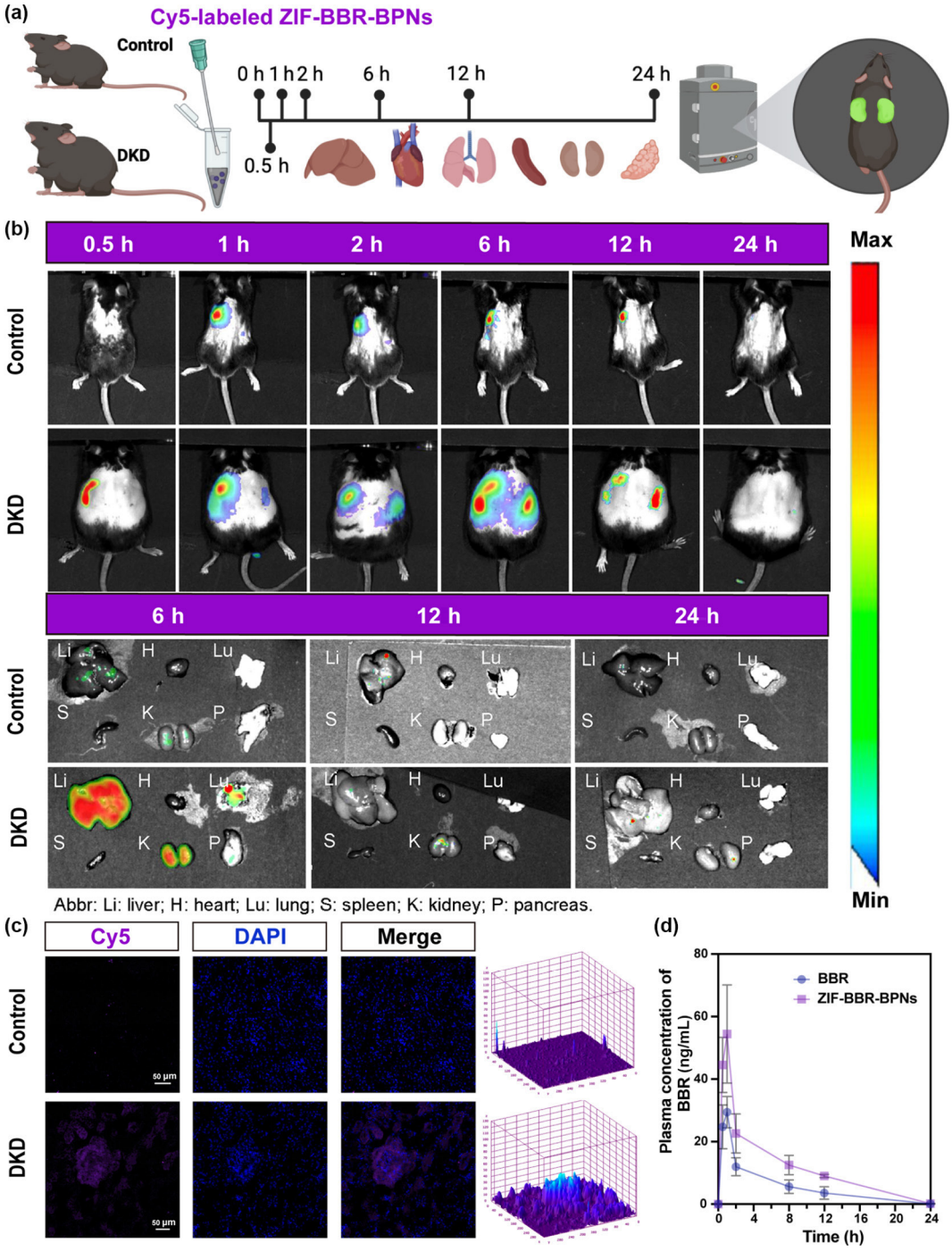

Figure 5 *In vivo* and *ex vivo* fluorescence distribution of Control and DKD mice following oral gavage of Cy5-labeled ZIF-BBR-BPNs. (a) Schematic illustration of the experimental design. Control and DKD mice were orally gavaged with Cy5-labeled ZIF-BBR-BPNs, and *in vivo* fluorescence imaging was performed at 0.5, 1, 2, 6, 12, and 24 h post-gavage. The organs analyzed include liver (Li), heart (H), lung (Lu), spleen (S), kidney (K), and pancreas (P). (b) Upper section: *In vivo* fluorescence imaging of Control and DKD mice at 0.5, 1, 2, 6, 12, and 24 h after oral gavage of Cy5-labeled ZIF-BBR-BPNs. Lower section: *Ex vivo* fluorescence imaging of isolated organs (Li, H, Lu, S, K, P) from Control and DKD mice at 6, 12, and 24 h post-gavage. (c) Fluorescence imaging of kidney tissue sections (6 h post-gavage) from Control and DKD mice: Cy5 channel (visualizing Cy5-labeled ZIF-BBR-BPNs), DAPI channel (staining cell nuclei), and Merge channel (overlap of Cy5 and DAPI signals). The right panels show the corresponding fluorescence intensity distribution spectra of the kidney tissue sections. (d) Plasma concentration-time profile of BBR after oral administration of free BBR and ZIF-BBR-BPNs.

interpretation is further supported by our *in vitro* findings, in which ZIF-BBR-BPNs more effectively alleviated cellular injury under oxidative and metabolic stress conditions, suggesting that improved drug exposure and formulation-enabled stabilization jointly contribute to the amplified renoprotective effects observed *in vivo*. Compared with free BBR, this superior efficacy is likely attributable to several formulation-related advantages. Encapsulation within the ZIF framework helps protect BBR from premature degradation during oral delivery, while the EGCG-based surface modification improves stability in the gastric environment and may provide

additional antioxidant support. Together, these features help explain the enhanced therapeutic performance of ZIF-BBR-BPNs in DKD mice.

3.5 Attenuation of renal inflammation, fibrosis, and endothelial injury by ZIF-BBR-BPNs

To clarify the mechanistic basis of the renoprotective effects of ZIF-BBR-BPNs, we examined renal inflammation, fibrosis, and associated molecular pathways in db/db mice. Immunohistochemical staining and quantitative analysis revealed marked upregulation of the macrophage marker F4/80 and the adhesion molecule intercellular adhesion molecule-1 (ICAM-1) in db/db kidneys, indicating enhanced inflammatory infiltration and endothelial activation (Figs. 6(a) and 6(b)). In parallel, fibrosis-associated markers, including Collagen IV and α-SMA, were substantially increased, reflecting progressive fibrotic remodeling.

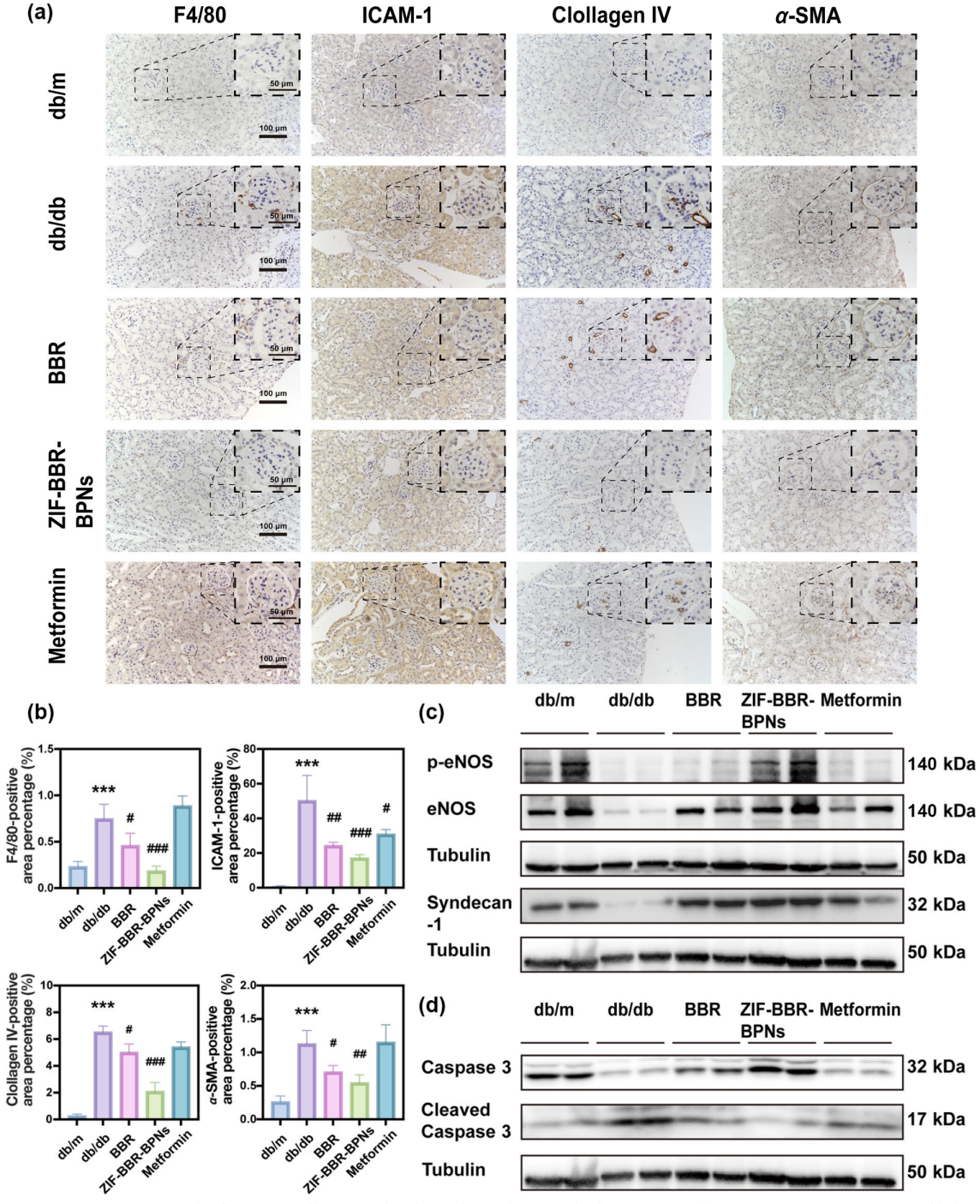

Figure 6 ZIF-BBR-BPNs attenuate renal inflammation, fibrosis, and pathway dysregulation in db/db DKD mice. (a) Representative IHC staining of kidney sections for F4/80, ICAM-1, Collagen IV, and α-SMA in db/m, db/db, and db/db mice treated with BBR, ZIF-BBR-BPNs, or metformin. Insets show enlarged boxed regions (scale bars: 100 μm). (b) Quantification of positive staining area (%; mean ± SD). ***$P < 0.001$ vs. db/m; $^{\#}P < 0.05$, $^{\#\#}P < 0.01$, and $^{\#\#\#}P < 0.001$ vs. db/db. (c) Representative Western blots of p-eNOS, eNOS, and Syndecan-1 in renal tissues (β-tubulin loading control). (d) Representative Western blots of Caspase 3 and Cleaved Caspase 3 in renal tissues (β-tubulin loading control).

Treatment with ZIF-BBR-BPNs robustly suppressed all of these markers, showing significantly greater attenuation of renal inflammation and fibrosis than free BBR or metformin. At the molecular level, Western blot analysis demonstrated pronounced reductions in phosphorylated eNOS, total eNOS, and the glomerular endothelial glycocalyx marker Syndecan-1 in db/db kidneys (Fig. 6(c)), consistent with endothelial dysfunction and glycocalyx disruption. Notably, ZIF-BBR-BPNs effectively restored the expression of these proteins (Figs. S9(a)–S9(c) in the ESM), indicating preservation of endothelial function and structural integrity. In parallel, db/db kidneys exhibited a marked increase in cleaved Caspase-3, indicative of enhanced apoptotic activity, which was significantly reversed following ZIF-BBR-BPNs treatment (Fig. 6(d) and Fig. S10 in the ESM), supporting a protective effect against renal cell apoptosis.

These *in vivo* molecular and histological improvements are consistent with our earlier *in vitro* findings under oxidative and metabolic stress conditions and align with the observed *in vivo* distribution behavior of ZIF-BBR-BPNs. The enhanced therapeutic efficacy of ZIF-BBR-BPNs can be attributed, at least in part, to the improved pharmacokinetic profile conferred by the ZIF-based nanoformulation, which increases systemic exposure and enables sustained renal presence of BBR.

The favorable *in vivo* behavior of ZIF-BBR-BPNs may also be related to the gradual disassembly of the nanoplatform during gastrointestinal transit and/or after systemic uptake, which could enable sustained release of berberine while allowing progressive degradation or clearance of the carrier components. Such a process may contribute to the improved systemic exposure and prolonged therapeutic activity observed in the present study. The detailed *in vivo* fate of the ZIF core and EGCG-based shell, however, remains to be further clarified. This prolonged availability may amplify the intrinsic anti-inflammatory, antifibrotic, and cytoprotective actions of BBR, thereby contributing to the pronounced mitigation of renal injury observed in DKD mice. A limitation of this study is that uncoated ZIF-BBR and EGCG-alone control groups were not included in the *in vivo* efficacy experiments. As a result, while our findings support the therapeutic advantage of the integrated ZIF-BBR-BPN system, the independent contribution of the EGCG-based coating to the enhanced *in vivo* efficacy remains to be further clarified. In addition, EGCG itself may also contribute to the observed therapeutic effects through its intrinsic antioxidant and cytoprotective properties. Therefore, the superior efficacy of ZIF-BBR-BPNs may reflect not only improved delivery and stability of BBR, but also a potential supportive contribution from the EGCG-based surface modification. Collectively, these findings indicate that ZIF-BBR-BPNs exert multifaceted renoprotection by simultaneously suppressing inflammation and fibrosis, preserving endothelial integrity, and inhibiting apoptosis.

3.6 Renoprotective mechanisms and biocompatibility of ZIF-BBR-BPNs in DKD

These *in vivo* molecular and histological improvements align with our earlier *in vitro* findings under oxidative and metabolic stress conditions, supporting the observed *in vivo* distribution behavior of ZIF-BBR-BPNs. The enhanced therapeutic efficacy of ZIF-BBR-BPNs can be attributed to the improved pharmacokinetic profile conferred by the ZIF-based nanoformulation (represented as purple polyhedrons in Fig. 7(a)), which increases systemic exposure and enables sustained renal presence of BBR.

This prolonged renal availability of BBR (delivered by ZIF-BBR-BPNs) amplifies its bioactivities via several mechanisms: Initially, it reduces ROS overproduction, normalizing the expression of apoptosis-related molecules by up-regulating the anti-apoptotic protein BCL2 and down-regulating the pro-apoptotic protein BAX. This leads to the inhibition of cytochrome C release and subsequent Caspase 3 activation, thereby preventing glomerular endothelial cell apoptosis. Additionally, ZIF-BBR-BPNs upregulate eNOS expression, restoring nitric oxide production and alleviating ROS-induced endothelial dysfunction. The nanoformulation also suppresses the activation of nuclear factor-kappa B (NF-κB), attenuating inflammation. Beyond these effects, ZIF-BBR-BPNs contribute to a reduction in fibrosis, partly by modulating α-SMA expression, which is associated with fibroblast activation in renal tissue. This is further supported by a reduction in ICAM-1 expression and mitigation of hyperglycemia, lipid accumulation, and elevated pro-inflammatory cytokines (IL-1β and TNF-α) in the glomerular vascular lumen. Moreover, ZIF-BBR-BPNs help lower blood glucose levels, reduce lipid accumulation, and improve the circulation of inflammatory factors, collectively enhancing the anti-inflammatory and antifibrotic efficacy of BBR. Additionally, the nanoformulation upregulates Syndecan-1, preserving the integrity of the renal barrier. This sustained availability of BBR enhances its intrinsic anti-inflammatory, antifibrotic, and cytoprotective actions, significantly contributing to the mitigation of renal injury observed in DKD mice. Collectively, these findings highlight that ZIF-BBR-BPNs provide multifaceted renoprotection by simultaneously suppressing inflammation and fibrosis, preserving endothelial integrity, and inhibiting apoptosis.

To further assess the clinical potential of ZIF-BBR-BPNs, we evaluated their biocompatibility in normal db/m mice, focusing on vital organ function, systemic inflammation, and histopathological integrity. The experimental design for this evaluation is outlined in Fig. S11 in the ESM. Mice received either a single oral dose of ZIF-BBR-BPNs (BBR-equivalent doses of 50, 100, or 200 mg/kg) with sample collection at 24 h, or daily administration for 4 weeks, followed by endpoint analysis. Throughout both phases, all mice showed normal behavior, stable body weight, and no mortality. Serum biochemical analysis demonstrated that neither single nor repeated dosing caused significant changes in liver function markers (alanine aminotransferase (ALT), aspartate aminotransferase (AST)) or renal function indicators (BUN, serum creatinine) at any dose level ($P > 0.05$ vs. control; Fig. 7(b)). Additionally, after 4 weeks of treatment, serum levels of pro-inflammatory cytokines (IL-1β, IL-6 and TNF-α) remained comparable to controls ($P > 0.05$; Fig. 7(c)), indicating no induction of chronic systemic inflammation. Histopathological analysis supported these findings, showing normal tissue architecture in major organs (heart, liver, spleen, lung, kidney, pancreas) with no signs of inflammation, necrosis, fibrosis, or structural abnormalities, both 24 h after a single dose (Fig. 7(d)) and after 4 weeks of repeated dosing (Fig. 7(e)). These results demonstrate that ZIF-BBR-BPNs exhibit excellent biocompatibility in healthy db/m mice. The absence of adverse effects on organ function, systemic inflammation, and tissue integrity — even at high doses and with prolonged administration — provides strong preclinical evidence for their favorable safety profile, supporting their potential for clinical translation in DKD therapy.

4 Conclusions

Collectively, these findings suggest that ZIF-BBR-BPNs may provide an effective nano-enabled approach for DKD. By

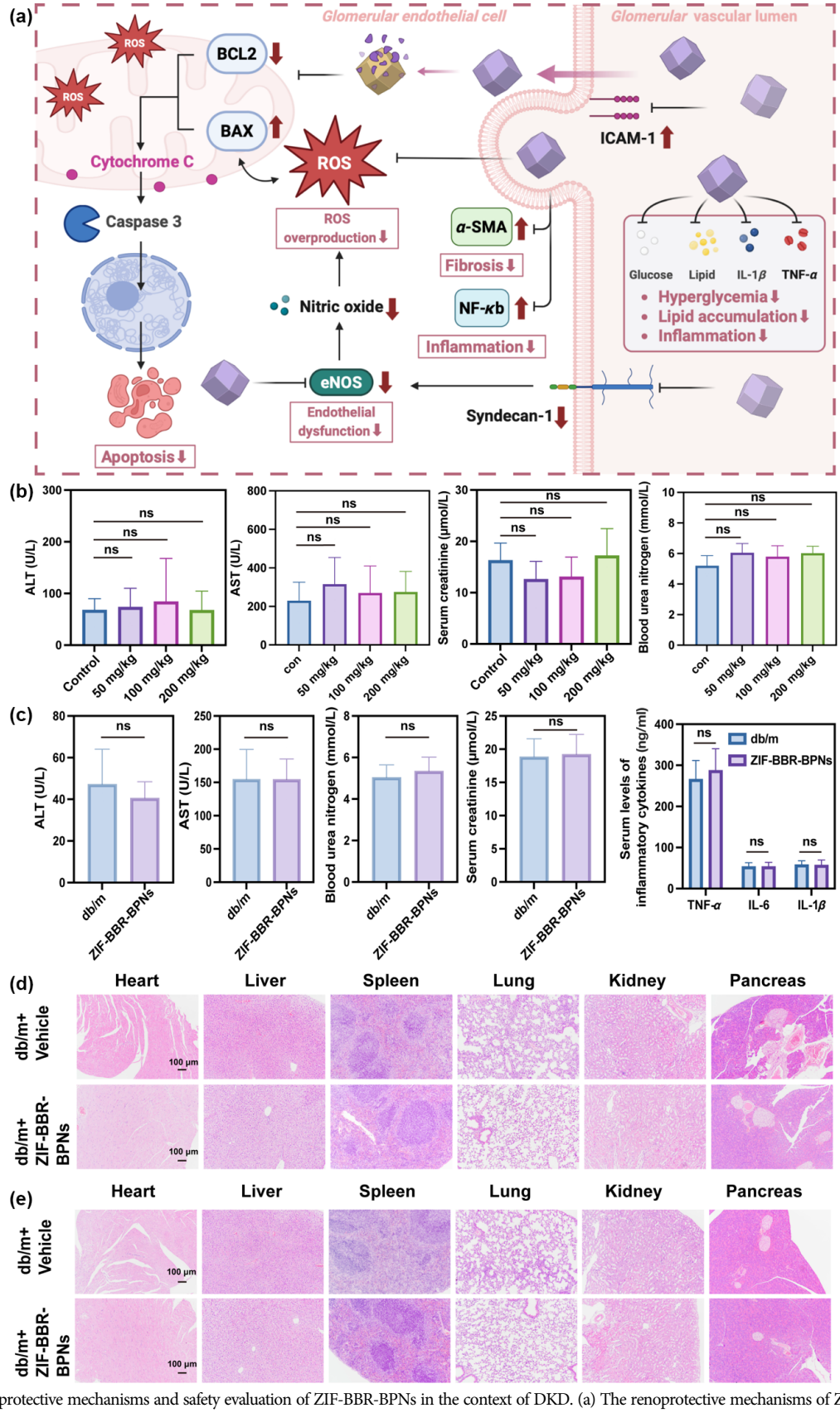

Figure 7 The renoprotective mechanisms and safety evaluation of ZIF-BBR-BPNs in the context of DKD. (a) The renoprotective mechanisms of ZIF-BBR-BPNs in the context of DKD. Acute and chronic toxicity evaluation of ZIF-BBR-BPNs in db/m mice: (b) Acute serum biochemistry (24 h): ALT, AST, BUN, and serum creatinine. (c) Chronic endpoints (4 weeks): ALT, AST, BUN, creatinine, and inflammatory cytokines, including IL-1*β*, IL-6, and TNF-*α*. (d) Representative H&E staining of major organs (heart, liver, spleen, lung, kidney, and pancreas) after acute dosing (scale bars: 100 μm). (e) Representative H&E staining of major organs after chronic dosing (scale bars: 100 μm). Data are presented as mean ± SD ($n = 6$). ns., no significant difference compared with the control group ($P > 0.05$).

encapsulating BBR in a zeolitic imidazolate framework and coating it with EGCG, this nanoparticle system significantly enhances the stability, bioavailability, and renal accumulation of BBR. The multi-targeted effects of BBR, including antioxidant, anti-inflammatory, and anti-apoptotic actions, are amplified by ZIF-BBR-BPNs, resulting in substantial improvements in renal function and reductions in inflammation, fibrosis, and glomerular injury in DKD mouse models. Furthermore, ZIF-BBR-BPNs demonstrate superior efficacy compared with free BBR and metformin, providing a more effective and holistic approach to DKD management. Together, these results support ZIF-BBR-BPNs as a promising oral nanoplatform for DKD therapy, with potential translational value for improving the delivery and therapeutic performance of natural compounds in chronic kidney disease. Further studies on long-term safety, formulation scalability, and *in vivo* fate will help advance its future clinical translation.

Electronic Supplementary Material: Supplementary material (detailed SEM/TEM micrographs, standard calibration curves, FTIR and XPS spectra, as well as quantitative data for apoptosis and Western blot analysis) is available in the online version of this article at https://doi.org/10.26599/NR.2026.94908761.

Data availability

All data needed to support the conclusions in the paper are presented in the manuscript and the Electronic Supplementary Material. Additional data related to this paper may be requested from the corresponding author upon request.

Acknowledgements

This study was supported by the Major projects of Sichuan Provincial Natural Science Foundation (No. 2025ZNSFSC0006, F. L. received this award) and the Natural Science Foundation of Sichuan Province (No. 24NSFSC6584, Z. P. G. received this award).

Declaration of competing interest

The authors declare no conflict of interest.

Author contribution statement

H. J. Z. and Y. T. Z. conceived and designed the study, performed the experiments, analyzed the data, and drafted the manuscript. M. G., M. X. W., H. Y. W., Q. Y., X. Y. L., X. T. C., and X. T. Z. contributed to data collection, experimental analysis, and visualization. Y. W. L., Z. P. G., and F. L. were responsible for the overall study design, supervision, and the critical review and editing of the manuscript. The manuscript was written through contributions of all authors. All authors have given approval to the final version of the manuscript.

Informed consent

Not applicable.

Ethics statement

All animal experiments were performed in accordance with the guidelines of the national and local authorities and were approved by the Laboratory Animal Ethics Committee of West China Hospital, Sichuan University (Approval No. 20250808006). The study followed the ARRIVE guidelines for the reporting of animal research.

Use of AI statement

None.

References

[1] Martinez Leon, V.; Hilburg, R.; Susztak, K. Mechanisms of diabetic kidney disease and established and emerging treatments. *Nat. Rev. Endocrinol.* **2026**, *22*, 21–35.

[2] American Diabetes Association Professional Practice Committee. Chronic kidney disease and risk management: Standards of care in diabetes-2025. *Diabetes Care* **2025**, *48*, S239–S251.

[3] Duncan, B. B.; Magliano, D. J.; Boyko, E. J. IDF diabetes atlas 11th edition 2025: Global prevalence and projections for 2050. *Nephrol. Dial. Transplant.* **2026**, *41*, 7–9.

[4] Kidney Disease: Improving Global Outcomes (KDIGO) CKD Work Group. KDIGO 2024 clinical practice guideline for the evaluation and management of chronic kidney disease. *Kidney Int.* **2024**, *105*, S117–S314.

[5] Alicic, R. Z.; Neumiller, J. J.; Galindo, R. J.; Tuttle, K. R. Use of glucose-lowering agents in diabetes and CKD. *Kidney Int. Rep.* **2022**, *7*, 2589–2607.

[6] Cleveland, K. H.; Schnellmann, R. G. Pharmacological targeting of mitochondria in diabetic kidney disease. *Pharmacol. Rev.* **2023**, *75*, 250–262.

[7] van Raalte, D. H.; Bjornstad, P.; Cherney, D. Z. I.; de Boer, I. H.; Fioretto, P.; Gordin, D.; Persson, F.; Rosas, S. E.; Rossing, P.; Schaub, J. A. et al. Combination therapy for kidney disease in people with diabetes mellitus. *Nat. Rev. Nephrol.* **2024**, *20*, 433–446.

[8] Gerardo González-González, J.; Cesar Solis, R.; Díaz González-Colmenero, A.; Raygoza-Cortez, K.; Moreno-Peña, P. J.; Sánchez, A. L.; McCoy, R. G.; Singh Ospina, N.; Maraka, S.; Brito, J. P. et al. Effect of metformin on microvascular outcomes in patients with type 2 diabetes: A systematic review and meta-analysis. *Diabetes Res. Clin. Pract.* **2022**, *186*, 109821.

[9] Yerevanian, A.; Soukas, A. A. Metformin: Mechanisms in human obesity and weight loss. *Curr. Obes. Rep.* **2019**, *8*, 156–164.

[10] Tuttle, K. R.; Agarwal, R.; Alpers, C. E.; Bakris, G. L.; Brosius, F. C.; Kolkhof, P.; Uribarri, J. Molecular mechanisms and therapeutic targets for diabetic kidney disease. *Kidney Int.* **2022**, *102*, 248–260.

[11] Ricciardi, C. A.; Gnudi, L. Kidney disease in diabetes: From mechanisms to clinical presentation and treatment strategies. *Metabolism* **2021**, *124*, 154890.

[12] Rayego-Mateos, S.; Rodrigues-Diez, R. R.; Fernandez-Fernandez, B.; Mora-Fernández, C.; Marchant, V.; Donate-Correa, J.; Navarro-González, J. F.; Ortiz, A.; Ruiz-Ortega, M. Targeting inflammation to treat diabetic kidney disease: The road to 2030. *Kidney Int.* **2023**, *103*, 282–296.

[13] Chen, Y. W.; Zhao, L.; Song, X. J.; Zhang, J. J.; Zhang, M. P.; Yang, D. L.; Jiao, A. H. Glucose-responsive injectable hydrogel for enhanced sonodynamic-antibacterial cascade therapy of diabetic abscess. *Adv. Funct. Mater.* **2026**, *36*, e14543.

[14] Liu, Z. R.; Huang, T.; Hong, Y.; Yang, Y. Q.; Chen, W. S.; Zeng, Q. T.; Chen, Q. H.; Yang, Y. Q.; Ying, X. H.; Zeng, W. et al. Adaptive antioxidant nanomedicines inhibit ferroptosis in renal tubular epithelial cells to alleviate diabetic kidney disease. *Adv. Sci.* **2025**, *12*, e05168.

[15] Hu, S. Y.; Wang, J. D.; Liu, E.; Zhang, X. M.; Xiang, J. Y.; Li, W.; Wei, P. F.; Zeng, J. H.; Zhang, Y.; Ma, X. Protective effect of berberine in diabetic nephropathy: A systematic review and meta-

analysis revealing the mechanism of action. *Pharmacol. Res.* **2022**, *185*, 106481.
[16] Tang, G. Y.; Li, S.; Zhang, C.; Chen, H. Y.; Wang, N.; Feng, Y. B. Clinical efficacies, underlying mechanisms and molecular targets of Chinese medicines for diabetic nephropathy treatment and management. *Acta Pharm. Sin. B* **2021**, *11*, 2749–2767.
[17] Zhou, W. H.; Asif, A.; Situ, C.; Wang, J. H.; Hao, H. H. Multiple target and regulatory pathways of berberine. *Phytomedicine* **2025**, *146*, 157030.
[18] Wang, K. J.; Yin, J.; Chen, J. Y.; Ma, J.; Si, H. B.; Xia, D. Q. Inhibition of inflammation by berberine: Molecular mechanism and network pharmacology analysis. *Phytomedicine* **2024**, *128*, 155258.
[19] Fan, Z. Y.; Wei, X. J.; Zhu, X. Y.; Yang, K.; Tian, L.; Wang, X. Y.; Du, Y. J.; Yang, L. M. Unveiling the therapeutic potential of berberine: Its therapeutic role and molecular mechanisms in kidney diseases. *Front. Pharmacol.* **2025**, *16*, 1549462.
[20] Qin, X.; Zhao, Y.; Gong, J.; Huang, W. Y.; Su, H.; Yuan, F.; Fang, K.; Wang, D. K.; Li, J. B.; Zou, X. et al. Berberine protects glomerular podocytes via inhibiting drp1-mediated mitochondrial fission and dysfunction. *Theranostics* **2019**, *9*, 1698–1713.
[21] Qin, X.; Jiang, M.; Zhao, Y.; Gong, J.; Su, H.; Yuan, F.; Fang, K.; Yuan, X. Y.; Yu, X.; Dong, H. et al. Berberine protects against diabetic kidney disease via promoting PGC-1α-regulated mitochondrial energy homeostasis. *Br. J. Pharmacol.* **2020**, *177*, 3646–3661.
[22] Nie, R. Y.; Yuan, Z. T.; Wu, Y. Z.; Pan, M. Q.; Lu, J. D.; Xiong, G. L. Time-dose response and mechanistic specificity of berberine in renal fibrosis from a multi-model integration perspective: A systematic review and meta-analysis on animal models. *Front. Pharmacol.* **2025**, *16*, 1600408.
[23] Wang, S. J.; Ren, H. H.; Zhong, H. Z.; Zhao, X. J.; Li, C. K.; Ma, J.; Gu, X. J.; Xue, Y. M.; Huang, S.; Yang, J. L. et al. Combined berberine and probiotic treatment as an effective regimen for improving postprandial hyperlipidemia in type 2 diabetes patients: A double blinded placebo controlled randomized study. *Gut Microbes* **2022**, *14*, 2003176.
[24] Harrison, S. A.; Gunn, N.; Neff, G. W.; Kohli, A.; Liu, L. P.; Flyer, A.; Goldkind, L.; Di Bisceglie, A. M. A phase 2, proof of concept, randomised controlled trial of berberine ursodeoxycholate in patients with presumed non-alcoholic steatohepatitis and type 2 diabetes. *Nat. Commun.* **2021**, *12*, 5503.
[25] Pan, L. B.; Yu, H.; Fu, J.; Hu, J. C.; Xu, H.; Zhang, Z. W.; Bu, M. M.; Yang, X. Y.; Zhang, H. J.; Lu, J. Y. et al. Berberine ameliorates chronic kidney disease through inhibiting the production of gut-derived uremic toxins in the gut microbiota. *Acta Pharm. Sin. B* **2023**, *13*, 1537–1553.
[26] Zhang, Y. F.; Gu, Y. Y.; Ren, H. H.; Wang, S. J.; Zhong, H. Z.; Zhao, X. J.; Ma, J.; Gu, X. J.; Xue, Y. M.; Huang, S. et al. Gut microbiome-related effects of berberine and probiotics on type 2 diabetes (the PREMOTE study). *Nat. Commun.* **2020**, *11*, 5015.
[27] Han, Y. F.; Xiang, Y. N.; Shi, Y.; Tang, X.; Pan, L.; Gao, J.; Bi, R. H.; Lai, X. R. Pharmacokinetics and pharmacological activities of berberine in diabetes mellitus treatment. *Evid. Based Complement. Alternat. Med.* **2021**, *2021*, 9987097.
[28] Ai, X. P.; Yu, P. L.; Peng, L. X.; Luo, L. L.; Liu, J.; Li, S. Q.; Lai, X. R.; Luan, F.; Meng, X. L. Berberine: A review of its pharmacokinetics properties and therapeutic potentials in diverse vascular diseases. *Front. Pharmacol.* **2021**, *12*, 762654.
[29] Kheir, M. M.; Wang, Y. G.; Hua, L.; Hu, J.; Li, L. L.; Lei, F.; Du, L. J. Acute toxicity of berberine and its correlation with the blood concentration in mice. *Food Chem. Toxicol.* **2010**, *48*, 1105–1110.
[30] He, S. S.; Li, X. Y.; He, Y. Y.; Guo, L.; Dong, Y. Z.; Wang, L. L.; Yang, L.; Li, L.; Huang, S. Y.; Fu, J. L. et al. High-density lipoprotein nanoparticles spontaneously target to damaged renal tubules and alleviate renal fibrosis by remodeling the fibrotic niches. *Nat. Commun.* **2025**, *16*, 1061.
[31] Kong, Y.; Chen, X.; Liu, F.; Tang, J. G.; Zhang, Y. J.; Zhang, X. X.; Zhang, L. Y.; Zhang, T.; Wang, Y. Q.; Su, M. X. et al. Ultrasmall polyphenol-NAD^+ nanoparticle-mediated renal delivery for mitochondrial repair and anti-inflammatory treatment of AKI-to-CKD progression. *Adv. Mater.* **2024**, *36*, 2310731.
[32] Xuan, C.; Chen, D. H.; Zhang, S. N.; Li, C. F.; Fang, Q. Y.; Chen, D. H.; Liu, J. B.; Jiang, X.; Zhang, Y. J.; Shen, W. J. et al. Isoquercitrin alleviates diabetic nephropathy by inhibiting STAT3 phosphorylation and dimerization. *Adv. Sci.* **2025**, *12*, 2414587.
[33] Mirhadi, E.; Rezaee, M.; Malaekeh-Nikouei, B. Nano strategies for berberine delivery, a natural alkaloid of *Berberis*. *Biomed. Pharmacother.* **2018**, *104*, 465–473.
[34] Bian, X. F.; Guo, Q.; Yau, L. F.; Yang, L.; Wang, X. Y.; Zhao, S. K.; Wu, S. Q.; Qin, X. R.; Jiang, Z. H.; Li, C. Berberine-inspired ionizable lipid for self-structure stabilization and brain targeting delivery of nucleic acid therapeutics. *Nat. Commun.* **2025**, *16*, 2368.
[35] Fu, S. Y.; Yi, X.; Li, Y.; Li, Y. H.; Qu, X. L.; Miao, P.; Xu, Y. Y. Berberine and chlorogenic acid-assembled nanoparticles for highly efficient inhibition of multidrug-resistant *Staphylococcus aureus*. *J. Hazard. Mater.* **2024**, *473*, 134680.
[36] Mourdikoudis, S.; Dutta, S.; Kamal, S.; Gómez-Graña, S.; Pastoriza-Santos, I.; Wuttke, S.; Polavarapu, L. State-of-the-art, insights, and perspectives for MOFs-nanocomposites and MOF-derived (nano)materials. *Adv. Mater.* **2025**, *37*, 2415399.
[37] Sun, J. C.; Zhao, Z. T.; Wei, X.; Yang, J. Z.; Li, D.; Li, M. L.; Choonara, Y. E.; Chen, L.; Ding, J. X.; Chen, X. S. Multi-bioactive poly(amino acid)-metal-organic framework nanocomposite for reinforced cascading photodynamic immunotherapy of cancer. *Biomaterials* **2026**, *324*, 123488.
[38] Xu, Y. J.; Chen, J.; Ding, J. X.; Sun, J.; Song, W. T.; Tang, Z. H.; Xiao, C. S.; Chen, X. S. Synthetic polymers for drug, gene, and vaccine delivery. *Polym. Sci. Technol.* **2025**, *1*, 171–220.
[39] Wang, H. Z.; Li, H. J.; Wang, X. L.; Ding, J. X. Immunologically effective chiral polymers to potentiate anti-cancer immune responses. *Polym. Sci. Technol.* **2025**, *1*, 809–811.
[40] Luo, Q.; Sun, J. F.; Li, Z. B.; Liu, B.; Ding, J. X. Thermo-sensitive poly(amino acid) hydrogel mediates cytoprotection through an antioxidant mechanism. *Chin. Chem. Lett.* **2025**, *36*, 110433.
[41] Sahu, K. P.; Singh, S.; Singh, A. K.; Azad, U. P.; Yadav, D.; Kumar, V.; Singh, S. K. Nanomaterials via ZIF-8: Preparations, catalytic and drug delivery applications. *Chem. Eng. J.* **2025**, *508*, 160663.
[42] Zhang, H. T.; Yuan, S. G.; Zheng, B. Y.; Wu, P.; He, X. M.; Zhao, Y.; Zhong, Z. F.; Zhang, X. F.; Guan, J.; Wang, H. J. et al. Lubricating and dual-responsive injectable hydrogels formulated from ZIF-8 facilitate osteoarthritis treatment by remodeling the microenvironment. *Small* **2025**, *21*, 2407885.
[43] Hadi, M. K.; Wang, X. Y.; Peng, Y. Y.; Sangaraju, S.; Ran, F. Functional polymeric membrane materials: A perspective from versatile methods and modification to potential applications. *Polym. Sci. Technol.* **2025**, *1*, 366–412.
[44] Liang, K.; Ricco, R.; Doherty, C. M.; Styles, M. J.; Bell, S.; Kirby, N.; Mudie, S.; Haylock, D.; Hill, A. J.; Doonan, C. J. et al. Biomimetic mineralization of metal-organic frameworks as protective coatings for biomacromolecules. *Nat. Commun.* **2015**, *6*, 7240.
[45] Gong, J. L.; Wang, H.; Xie, C. M.; Dai, Y. G.; Wang, Y. R.; Guo, W. H. A multifunctional injectable hydrogel for boosted diabetic wound healing assisted by Quercetin-ZIF system. *Chem. Eng. J.* **2024**, *495*, 153425.
[46] Li, W. H.; Zhong, J. T.; Wang, X.; Zhuang, W. D.; Yang, Y. P.; He, P. P.; Alswadeh, M.; Li, C. R.; Li, X. Y.; Hu, N. et al. Intelligent

responsive zeolitic imidazolate framework-8@copper oxide nanocomposite 3D-printed scaffolds for efficient repair of infected bone defects. *ACS Nano* **2025**, *19*, 35154–35180.

[47] Yang, H. H.; Luan, Q.; Guan, W. L.; Nong, W. Q. Oral delivery systems of dietary bioactive compounds based on metal-organic frameworks: A review. *Compr. Rev. Food Sci. Food Saf.* **2025**, *24*, e70272.

[48] Sun, Y. Y.; Ye, X. T.; Yang, L.; Dong, S.; Chen, C.; Wang, Y. N.; Qiao, J. N.; Liu, C. Y.; Liu, Y. P.; Chen, Y. Oral microbiota-responsive ZIF nanoplatform via double-layer glycans modified combined with PD-1 inhibitor for treatment of microsatellite-stable colorectal cancer. *Mater. Today Bio* **2025**, *35*, 102565.

[49] Zeng, X.; Wang, Z. Z.; Zhao, A.; Wu, Y. Q.; Wang, Z. P.; Wu, A. W.; Wang, Q.; Xia, X.; Chen, X. C.; Zhao, W. et al. Zinc nanoparticles from oral supplements accumulate in renal tumours and stimulate antitumour immune responses. *Nat. Mater.* **2025**, *24*, 287–296.

[50] Ji, W.; Zhang, P.; Zhou, Y. G.; Zhou, X. Q.; Ma, X. F.; Tan, T. W.; Cao, H. Hydrogel-encapsulated medium chain lipid-modified zeolite imidazole framework-90 as a promising platform for oral delivery of proteins. *J. Control. Release* **2024**, *367*, 93–106.

[51] Wang, Z. Q.; Zhu, Y. X.; Sheng, H. X.; Cheng, Y.; Zhang, Y.; Yang, Y. F.; Huang, Z. X.; Chen, X. Y.; Qiu, Y. F.; Wu, R. et al. Self-assembling metal-polyphenol-protein nanocomplex enhancing islet graft survival and transplantation outcome. *Chem. Eng. J.* **2025**, *526*, 171188.

[52] Zhen, W. Y.; Liu, Y.; An, S. J.; Jiang, X. E. Glutathione-induced *in situ* michael addition between nanoparticles for pyroptosis and immunotherapy. *Angew. Chem., Int. Ed.* **2023**, *62*, e202301866.

[53] Zhang, J. H.; Zhong, J.; Liang, B.; Liu, W. J.; Zhang, H. J.; Wang, T. Y.; Huang, L. P.; Yang, L.; Gu, Z. P.; Li, Y. W. Robust injectable hydrogels for hemophilic arthropathy via anti-inflammation, iron removal and cartilage protection. *Adv. Funct. Mater.* **2025**, *35*, 2500271.

[54] Xu, Z. J.; Liu, G. T.; Zheng, L.; Wu, J. A polyphenol-modified chitosan hybrid hydrogel with enhanced antimicrobial and antioxidant activities for rapid healing of diabetic wounds. *Nano Res.* **2023**, *16*, 905–916.

[55] Wang, Y. N.; Zhang, J. W.; Zhao, Y.; Pu, M. J.; Song, X. Y.; Yu, L. M.; Yan, X. F.; Wu, J.; He, Z. Y. Innovations and challenges of polyphenol-based smart drug delivery systems. *Nano Res.* **2022**, *15*, 8156–8184.

[56] Cao, H.; Yang, L.; Tian, R.; Wu, H. X.; Gu, Z. P.; Li, Y. W. Versatile polyphenolic platforms in regulating cell biology. *Chem. Soc. Rev.* **2022**, *51*, 4175–4198.

[57] Wang, T. Y.; Guo, L. H.; Wu, S. W.; Xu, Y. Y.; Song, J. M.; Yang, Y.; Zhang, H. J.; Li, D. C.; Li, Y. W.; Jiang, X. et al. Polyphenolic platform ameliorated sanshool for skin photoprotection. *Adv. Sci.* **2024**, *11*, 2310012.

[58] Yang, P.; Huang, Q. Q.; Zhang, J. H.; Li, Y. W.; Gao, H. L.; Gu, Z. P. Natural polyphenolic nanodots for Alzheimer's disease treatment. *Adv. Mater.* **2024**, *36*, 2308393.

[59] Zhang, H. J.; Zhang, J. H.; Wang, T. Y.; Li, H. T.; Zhang, R.; Chen, X. C.; Gu, Z. P.; Li, Y. W. Visible light-responsive polyphenolic bio-glues for oral mucosal wound healing. *Adv. Funct. Mater.* **2024**, *34*, 2408462.

[60] Gao, X. Z.; Xu, Z. J.; Liu, G. T.; Wu, J. Polyphenols as a versatile component in tissue engineering. *Acta Biomater.* **2021**, *119*, 57–74.

[61] Liang, X. D.; Xian, C. H.; Du, J. Y.; Huang, X. L.; Yang, Y. G.; Bi, G.; Li, X. Z.; Gao, M.; Wu, M. S.; Wu, J. et al. Sprayable self-assembled curcumin-metal-polyphenol nanomedicine with anti-inflammatory, ROS-scavenging and pro-angiogenesis effects for promoting diabetic wound healing. *Nano Res.* **2025**, *18*, 94908001.